

# $2\pi$ spectrometer: A new apparatus for the investigation of ion surface interaction

V. A. Morosov, A. Kalinin, Z. Szilagy, M. Barat, and P. Roncin  
*Laboratoire des Collisions Atomiques et Moléculaires, Bat 351, Université Paris Sud,  
Orsay Cedex F 91405, France*

(Received 15 January 1996; accepted for publication 11 March 1996)

A new spectrometer for studying ion surface interaction is described. This apparatus is built around a secondary electron and ion detector with a very large acceptance angle and made of 16 individual microchannel plate detectors located on a half sphere. A simultaneous detection of the scattered projectiles with an additional position sensitive detector allows measurements of the correlation between all these particles using a multicoincidence technique. With this spectrometer, a large variety of measurements are possible such as the energy spectra of the secondary electrons as well as the statistics of the number of ejected electrons, the scattering pattern of the reflected projectiles and their charge-state distribution, the analysis of the sputtered ions. Some examples are given concerning the impact of multiply charged ions on a LiF single crystal. The dependence of the secondary electron multiplicity as a function of the charge state, of the surface channeling condition, and of the scattering angle of the reflected ion, is given as a type of information provided by the analysis of the correlation. © 1996 American Institute of Physics. [S0034-6748(96)05106-4]

## I. INTRODUCTION

The interaction of ions with a surface has been investigated using a large palette of tools. The case of the interaction of multiply charged ions (MCIs) is particularly significant. The impact of a highly charged ion on a metal surface gives rise to the emission of a huge number of slow electrons.<sup>1</sup> For instance, Aumayr *et al.*<sup>2</sup> have measured up to 250 electrons emitted after the impact of slow Th<sup>80+</sup> ions. Events of such multiplicity are not commonly encountered in atomic physics. Since this discovery, a large activity both theoretical and experimental has followed to understand the underlying mechanisms. The spectroscopy of secondary electrons was the most utilized technique but was mainly applied to the analysis of the high-energy Auger electrons emitted during the filling of the inner-shell vacancies of the MCI.<sup>3</sup> Complementary information was obtained with x-ray spectroscopy,<sup>4</sup> a technique mostly used with rather highly charged ions due to limitations introduced by the low fluorescence yield and practical difficulties in the soft x-ray spectroscopy. An interesting technique was developed by the Vienna group,<sup>5</sup> which was able, using a solid-state detector, to determine the distribution (statistics) of the number of ejected electrons. Finally, additional information has been gained by the analysis of the scattered particle. In particular, it has been shown that projectiles are mainly scattered as neutrals after the interaction with a metal surface.<sup>6</sup>

Our goal, in developing this new apparatus was to obtain new information by studying the correlation between the various particles which participate to the scattering process: secondary electrons, ions, and reflected projectiles. To our knowledge this technique, widely used to study the atomic interactions in gas phase, has scarcely been applied to ion surface interaction.<sup>7</sup> One of the problems which arises with coincidence technique, is the necessity to optimize the detection efficiency. In the present case, care should be taken to collect the maximum of secondary particles which are emitted in the  $2\pi$  steradians around the impact point. This leads

us to conceive a special detector of hemispherical shape,<sup>8</sup> a device which will be described here in detail. Several results will be presented to illustrate the versatility of this apparatus such as energy and angular distributions of secondary electrons and ions, as well as scattering profile, charge-state distribution and energy-loss spectra of the reflected projectiles. A special attention will be borne on correlation between electrons and ions.

## II. DESCRIPTION OF THE $2\pi$ SPECTROMETER

The present spectrometer (Fig. 1) is based on the combination of two detecting devices. The main detector, for which the name “ $2\pi$ ” has been given to our apparatus, has a hemispherical shape in order to optimize the angular detection efficiency in collecting secondary electrons or ions ejected by ion impacts on a surface located at the center of the sphere. On one side of the hemisphere, the incident beam is injected at grazing angle through a differentially pumped tube terminated by a  $\varnothing=100\ \mu\text{m}$  diaphragm. On the opposite side, the projectiles scattered in the  $\varnothing=20\ \text{mm}$  exit hole, are received, 200 mm away, onto a position sensitive detector (PSD) of  $\varnothing=40\ \text{mm}$  allowing determination of the scattering angle. A set of 2-mm-wide slits followed by deflecting plates can be inserted in between the  $2\pi$  detector output cone and the PSD to analyze the charge-state distribution of the scattered particles. This device can be lifted up to get the pattern of the scattered particles on the PSD. The sample holder allows azimuthal orientation of the target and control of the incidence angle with respect to the fixed direction of the incident beam around  $5^\circ$ . The manipulator also permits to expose the target to a commercial sputtering argon gun. The  $2\pi$  detector is located inside a  $\mu$ -metal chamber from Vacuum Generator Inc. pumped by a titanium sublimator and a 1000  $\ell/\text{s}$  turbomolecular pump. For security, heating has been limited below  $120^\circ\text{C}$ , and despite all the resistors and the large number of  $50\ \Omega$  coaxial cables, a  $3\times 10^{-10}$  mb base pressure has been obtained.

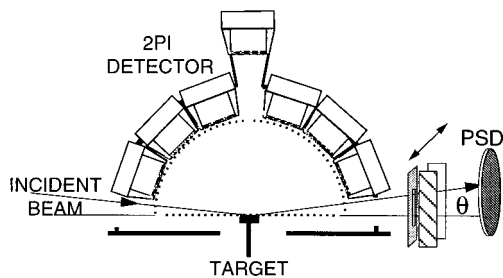


FIG. 1. Schematic representation of the spectrometer. The beam is injected at  $5^\circ$  incidence angle and scattered particles are detected on a position sensitive detector (PSD) centered on the direction of specular reflection. A set of slit and condensor plates can be inserted to allow charge-state analysis. The three rows of five detectors are schematized. They are located on a half sphere 6 cm away from the target. Notice the additional detector on the top of the sphere (10.5 cm from the target).

### A. Structure of the main detector

The main detector is made of an assembly of 16 units based on microchannel plates (MCP) located on a half sphere. The mapping of a complete sphere by disks is a well-known problem as, for example, the 32 sides of the isocahedral “buckyball,” but this is not the case for a half sphere since there is no equatorial plane in the above-mentioned structure. In our design, the compromise, was to favor detectors above the equatorial plane slightly reducing the effective surface around the equatorial plane. The selected design consists of three rows of five detectors leaving a smaller polar hole on the top (Fig. 1) available for an extra 16th detector or for beam injection at normal incidence. The 15 detectors are located between two concentric half spheres. The distance from the detector entrance planes to the sphere center is 6 cm whereas the topmost 16th detector is placed at a larger distance (10.5 cm) from the center. The 3-mm-thick outer sphere is designed to tightly hold the individual MCP detectors from their back side. The entrance sides of the 15 MCP detectors almost touch each other and define the inner half sphere. To avoid field penetration inside the half sphere, a hemispherical grid is required. Actually, the inner sphere is made of a thin frame (0.5 mm) of rings, each of which matches the entrance ring of the individual detectors. Each ring is covered by a high transparency 50- $\mu$ m-thick copper grid. This concentric sphere design leaves most of the space on the detector backside available for connections and tight holding, while the detectors are most densely packed on the active entrance side. This results in a geometrical coverage close to 50% of the hemisphere above the sample.

### B. Individual detectors

Most of the commercially available MCP detectors have a comparatively large total area relative to the active one. At variance our design, based on a conical structure is rather thick, but has an entrance diameter close to the MCP diameter. Each detector consists of two 32-mm-diam Russian MCP 0.5 mm thick mounted in chevron with an entrance ring ( $\varnothing_{in}=31$  mm and  $\varnothing_{ext}=35$  mm) allowing an active surface ratio of 80%. All electrical connections are located on the backside for easy wiring. Three hooks press the entrance

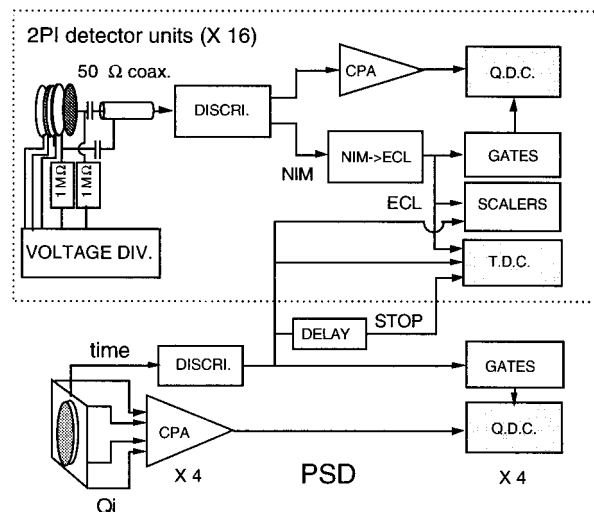


FIG. 2. Schematic of the electronics. The sixteen output of the subunits of the  $2\pi$  detector are sent to fast discriminators with both logic and analog outputs. The analog output is amplified by charge preamplifier (CPA) and sent to charge digitizer (QDC). The timing NIM output is converted to ECL standard which are used to trigger the proper channel of the multihit time digitizer (TDC) and to generate the integrating gate for the QDC. The time information from the PSD triggers one TDC channel and provides the common stop after a 20  $\mu$ s delay. The four charges out of the PSD collector are also amplified by CPA's and digitized by a QDC.

ring on three sapphire balls  $\varnothing=1.6$  mm and on the detector backside. The two MCP are sandwiched in between and pressed by a 100  $\mu$ m CuBe ring-shaped spring. A specific UHV 50  $\Omega$  connector has been designed with built-in 5 kV 100 pF isolation capacitors made of 50- $\mu$ m-thick kapton foil. Not only the signal is decoupled from the collector but also the coaxial shield of the signal cable is connected to the output of the second MCP to provide a local differential ground. To force the time signal into the 50  $\Omega$  cable, the collector and output of the second MCP are biased through a 1 M $\Omega$  UHV compatible resistor connected directly to the detector backside (Fig. 2). Each detector has five  $\varnothing=0.8$  mm pin connectors compatible with CuBe crimped female connectors (Ceramaseal 11288-02-X), three to control the two MCP voltages, one for the entrance ring and one for the collector bias. These wires are connected to adjustable voltage dividers outside the vacuum chamber. This allows fine tuning of each detector voltage and offers the possibility to bias each detector either for electron/negative ion or for positive ion detection. The sixteen 50  $\Omega$  UHV cables are connected to a double-sided SMA 50  $\Omega$  feedthrough welded on a CF100 flange.

## III. DATA ACQUISITION SYSTEM

### A. Scattered particle detection: The PSD detector

A schematic drawing of the electronics associated with the present spectrometer is shown in Fig. 2. The arrival time and impact localization of the scattered projectile onto the PSD is determined by a charge division technique using a two-dimensional resistive anode (Quantar Technology), either through standard pulse preamplifiers and linear pulse

shaping amplifiers coupled to a analog-to-digital voltage converters (ADC) or (as shown in Fig. 2) through low-cost charge preamplifiers (LeCroy 2724 card) directly coupled to a multichannel charge-to-digital converters (QDC 7176 Philips). The time pick-up signal is taken from the output of the second MCP, the positive polarity is reversed to negative by a pulse transformer and sent to a constant fraction discriminator. The time signal is then used both to “strobe” the ADC (or QDC) and to correlate the scattered ions signal from the PSD to the signals coming from the  $2\pi$  detector.

## B. The $2\pi$ detector

The signal from each detector of the  $2\pi$  device enters a constant fraction discriminator specially designed for MCP fast pulses; DGM0 manufactured by the IPNO (Institut de Physique Nucléaire d’Orsay IN2P3, Orsay Cedex F 91405). This device offers decisive advantages as a noise insensitivity below 100 kHz, a very low threshold (below 3 mV) allowing a wide dynamics associated with a very high time resolution reaching an ultimate value of 12 ps, much better than the overall resolution reached in our experiment. This device also includes a built-in high impedance linear amplifier which “regenerates” the entrance signal under 50  $\Omega$  load for pulse amplitude measurements. The time pick-up signal is then converted from NIM to ECL standard and sent through a 16-twisted pair flat cable to a multihit, multichannel time-to-digital converter (TDC 1176 by LeCroy) and to a 16-channel scaler (CAEN V560E) both located in a VME crate. The TDC records the arrival time of the 16 channels with a 1 ns resolution during a 64  $\mu$ s time window. In practice, a 7 ns resolution has been obtained with a dc beam, mainly limited by the scattered beam energy spread (see Sec. IV B and Fig. 5). There is no dead time between the various channels but a minimum time of 20 ns is required before a given channel can be hit again. This unit is operated in the common-stop mode. In the present experimental procedure, the stop signal is provided by the detection of the scattered projectile (PSD) delayed by some 10–20  $\mu$ s to allow for the detection, in coincidence, of slow sputtered ions by any of the  $2\pi$  detector units.

In order to adjust all detector units for comparable response, the pulse height distributions (PHD) are also measured. Notice, however, that in the future, such analysis in coincidence will allow identification of double hits on the same detector or, in case of sputtered ion detection, the PHD associated with the detection of a given ionic species would help in the determination of the corresponding detection efficiency. To measure the PHD, the signals from individual detectors, regenerated by the DGM0 and further amplified by a 24-channel charge preamplifier card (LeCroy 2427) are delayed by 32 ns cables before being digitized in a 16-channel individual gates charge-to-digital converter (Phillips QDC 7176). Each individual gate is built from the timing signal stretched to a 140 ns width whereas the “general conversion enable gate” is generated by a OR gate among all detector individual gates further stretched up to 2  $\mu$ s. The mean charge out of the MCP around 0.8 pC, is hardly larger than the noise level arising when coupling the two amplifiers. Of course, if the detector outputs are directly plugged into the

2427 preamplifier card, the resulting signals are virtually noise free but the time information is lost. In addition it is very difficult to correlated the charge value to a given time signal when a detector is hit more than once during the general gate. In the future, this situation may be improved by use of charge-to-time converter chips such as the MQT200 manufactured by LeCroy. Each hit on the detector would produce two time signals, the standard time signal followed by a second one separated from the first one proportionally to the charge produced by the MCP. If priority is given to short dead time, the two signals could be sent to two separate TDC channels. Otherwise, the start signal may be the leading edge of a signal of which the trailing edge is generated by the charge signal; only one TDC channel is then required. Such setup would allow multihit operations both for time and charge information with built-in correlations.

## C. Computer data processing control

Data “preprocessing” and master control of the various converters are handled by a VME card (Motorola MVME 167) equipped with a 33 MHz 68040 microprocessor. Presently, the preprocessing has been limited to the derivation of the XY scattered projectile positions and to the filtering out of the noncoincident events. The selected data are transmitted via a private “ethernet” link to a host workstation (HP 715-33) and to a 2 Gbytes tape recorder (4 mm DAT). Samples of data are randomly picked up to be further processed and displayed “on line” to control the experiment. The software connections between the UNIX operated workstation and the “VxWorks” operated VME master as well as the data display on the workstation and the storage in the tape are made transparent in the “OASIS” interface (“OASIS” for Open Acquisition Software is developed by the IPNO and Saturne CEA Saclay France). Only two small programs are to be written by the user, one which run in the VME host computer when an event trigger is received. It describes the succession of CAMAC and VME orders to be emitted for data readout and reset of the electronics. The second piece of code runs in the Workstation and does the data processing to construct and fill the histograms prior to display.

## D. Data structure and analysis procedure

Assuming, for example, that all 16 units of the  $2\pi$  detector are biased for electron detection, an “event,” defined as the impact of an ion on the surface, will be composed of  $n$  arrival times of the electrons and the corresponding pulse height distributions measured with the QDC on the 16 channels plus the arrival time and position of the scattered projectile. For the sake of simplicity, the present analysis disregards the pulse height measurements reducing the data to  $n+1$  time values and to the X,Y impact location of the scattered projectile. This already generates a  $n+3$ -dimensional space where correlations are to be looked for. So far, only specific one- or two-dimensional projections have been processed such as 2D scattering profiles of the reflected ion/neutrals associated with a given number of detected electron or with a selected energy gain. One word has to be said about

the time origin of the events. For fast enough projectiles, as 16 keV  $O^{8+}$  ions, and despite of the energy loss, the time spread of the scattered ion signal can be as narrow as 7 ns FWHM, allowing the resolution of the  $K$  and  $M$  Auger lines in the electron spectra triggered by the scattered ions (see Fig. 5). The impact time of the ions on the target can then be deduced from the known energy of the  $K$  electrons and from the distance between the target and the detectors. Notice that such  $K$  electrons are detected only for 1/4 of the events. In a second step, all times of flight can be recalibrated more accurately using this new time reference which, incidentally, can be used to measure the energy losses undergone by the scattered particle with 1 ns sensitivity. In the near future, the high efficiency of the “ $2\pi$ ” detector will also allow to work with a chopped incident beam, with an expected better energy resolution of the secondary particles.

#### IV. TYPICAL EXAMPLES OF RESULTS

Selected data are presented in this article to illustrate the type of information which can be gained using the present spectrometer. For the sake of clarity, data obtained for scattering of various ions  $O^{4+}$ ,  $O^{8+}$ , and  $Ar^{16+}$  at  $5^\circ$  incidence angle, on a same surface sample, a LiF(100) crystal is selected. Measurements with the multiply charged ions were made using the ECR source available at the AIM facilities in Grenoble. In all experiments, the primary beam intensity was kept below  $10^4$  ions per second ( $\approx 10^{-15} q$  A) and no charging up of the insulator target, even at room temperature, was found which could perturb the measurement.

##### A. Scattered particles

###### 1. Scattered profile

The scattering of  $Li^+$  particles on the PSD with the slit lifted up was first used to test the PSD detector. In particular, the so-called “banana” shape<sup>6</sup> of the scattered particle profile was clearly observed in channeling conditions (normal energy  $\approx 7$  eV). These data have been obtained with a 1 keV  $Li^+$  ion source ( $\beta$  eucryptite in a porous tungsten) placed at the entrance of the tube. The beam is then collimated by two holes resulting in a narrow beam having an angular spread  $\Delta\theta=0.1^\circ$  and giving a submillimetric spot on the PSD. The much wider spot of the scattered particles is related to the surface roughness. In fact, the spot becomes more and more narrow after several annealing and sputtering operations, providing a simple method to follow the construction of a flat atomic surface.<sup>9</sup>

###### 2. Charge-state analysis of the scattered particles

With the slit lifted down, the charge states of the scattered particles are analyzed by the electrostatic deflector (Fig. 1) giving on the PSD several images of the slit.<sup>6</sup> For each impact on the PSD, we receive the  $XY$  coordinates but also the pulse amplitude produced by the PSD. This is particularly useful to determine the relative detection efficiency when ions of different charge states are detected with eventually different kinetic energies. In our setup, the MCP collector was grounded, so that the scattered particles of charge  $q$  are post accelerated or decelerated by some 2.3q keV be-

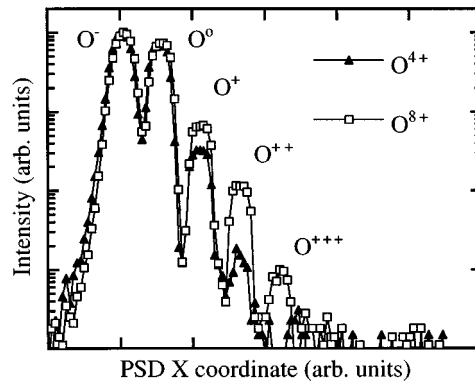


FIG. 3. Charge-state distribution of the oxygen scattered from the LiF surface. Open squares are for incident 16 keV  $O^{8+}$  ions and full triangles for 16 keV  $O^{4+}$  ions. The neutral and negative components have the same relative intensities whereas the positive fractions are much larger for  $O^{8+}$  ions as projectile.

tween the detector front grid and the first MCP located two mm away. If the total kinetic energy is high enough, we have checked that all final charge states are associated with the same pulse amplitude distribution. But this is not the case, for instance, when 4 keV ions are sent to the surface, then the singly charged negative and positive ions are decelerated to 1.7 keV or accelerated to 6.3 keV, respectively, in front of the MCP. In this case, the pulse amplitude distributions are different and are used to correct the relative detection efficiency to first order. It is often possible to find a proper scaling ratio between two different distributions. We can then evaluate the part of the distributions which has shifted below the discriminator threshold for each distribution.

In addition to the relative yield for the various charge states obtained by integrating the intensity for each image of the slit, one also get the angular profile for each charge state ( $\theta$  dependence), with the intensity variation along the length of the slit and also the azimuthal dependence  $\phi$  by lifting the slit along the  $z$  direction (see below). Figure 3 shows the charge-state dependence of a 16 keV beam of  $O^{8+}$  ions scattered by the LiF surface. The most striking feature is the dominance of the  $O^-$  peak, a result found by Auth *et al.*<sup>10</sup> Large negative ion fractions have also been obtained for a variety of atomic projectiles which have a stable negative ion. It is also noticeable that the negative ion yield is much higher with an insulator surface than with a conducting surface. An other interesting finding comes from the comparison of the charge-state dependence for impact of  $O^{8+}$  and  $O^{4+}$  ions of the same velocity. One notice that the two dominant peaks for neutrals and negative ions have the same relative intensity showing that the incident beam has “forgotten” its initial state before scattering as previously found for metals. On the other hand, the minor positive ionic components of the scattered beam have much higher intensities in the case of  $O^{8+}$ . This feature, already observed in the case of a metal surface by Meyer *et al.*<sup>6</sup> is due the survival of the initial  $K$ -shell vacancies. The angular profiles along  $\theta$  are displayed on Fig. 4 for the various final charge states with a 16 keV  $O^{8+}$  incident beam. These results show that the negative ions are scattered at the most grazing angle and that the

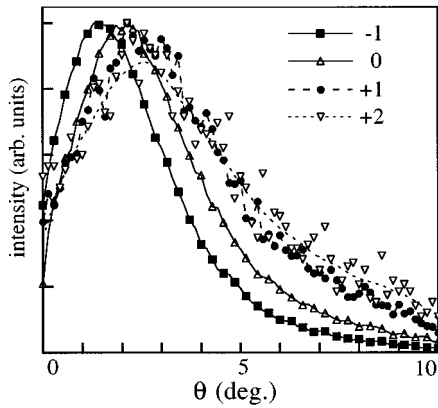


FIG. 4. Intensity profiles as a function of the scattering angle  $\theta$  (see the text and Fig. 1) for  $O^{8+}$  incident ions and for different charge states of the scattered particles. The negative ions are found at smaller scattering angle. Note that the target angular position is known with an accuracy of  $1^\circ$ .

scattering angle increases with charge state. In contrast, the relative abundance of the various charge states does not depend on the  $\Phi$  azimuthal angle. In case of metal surfaces, this behavior led to model where the velocity normal to the target is the key parameter.<sup>11</sup>

## B. Secondary electrons

### 1. Electron energy spectra

The energy of the secondary electrons is measured by time of flight (TOF). In a continuous beam experiment (unchopped), one must find an appropriate signal to trigger the TOF measurement. The main problem is then to define a time origin such as the unknown impact time in the present case. For example, in the spectra shown in Fig. 5, the arrival time  $t_{\text{scatt}}$  of the scattered particle has been chosen as the start signal. The time  $t_n - t_{\text{scatt}}$ , where  $t_n$  stands for the electron arrival time as measured by the TDC, is broadened by the scattered projectile energy loss distribution which, for high enough projectile velocity does not exceed 5 ns (for 32 keV oxygen projectile). The ion arrival time, although a stable time reference, does not give the time of the impact. The time origin can in fact be derived accurately by comparing the time of flight recorded on any detector on the half sphere

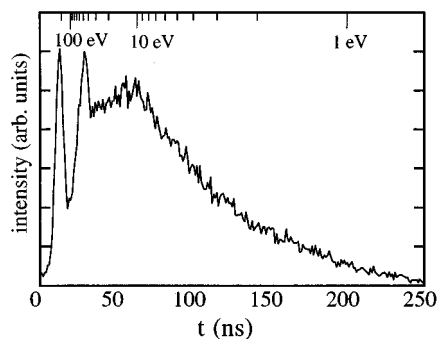


FIG. 5. Electron time of flight measured with the scattered particle as a time reference for 32 keV  $O^{8+}$  ions colliding on a LiF target. The two left-hand side peaks are ascribed to projectile  $K$  and  $L$  Auger electrons, respectively.

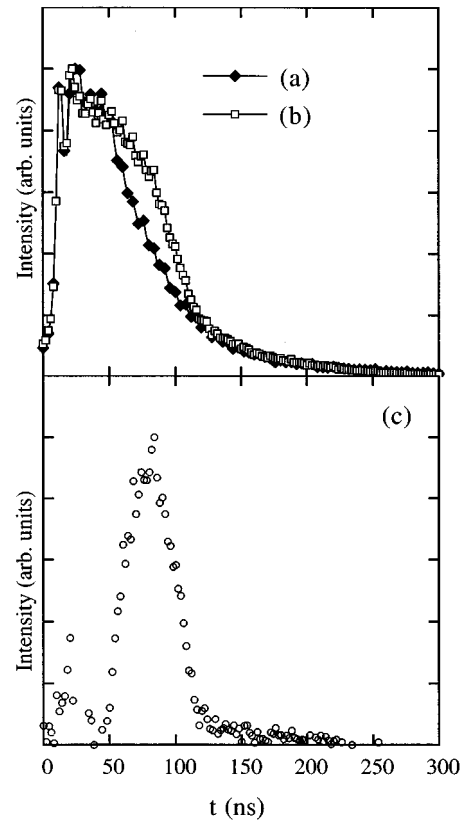


FIG. 6. Secondary electron time flight spectra for 32 keV  $O^{8+}$  ions on LiF target recorded on a detector placed (a) in the backward and (b) in the forward beam direction. Curve (c) shows the difference between the (b) and (a) distributions giving rise to a peak at an energy of 2 eV.

(located 6 cm from the target) with the time of flight recorded on the topmost detector located almost twice further. Fitting the two spectra with a known distance ratio immediately gives the time origin for both spectra, as well as the mean energy of the fastest electrons. Despite the time spread introduced by the energy spread of the ion, such spectra show three structures in the case of incident  $O^{8+}$  ions, the two narrow peaks corresponding to the fastest electrons are ascribed to the filling of  $K$  and  $L$  shell vacancies, respectively. These peaks are followed by a structureless tail stretching in the eV range. The simultaneous electron detection on all detectors allows the determination of the spatial and energy distributions of the secondary electrons. This distribution is found isotropic for the peaks assigned to projectile Auger emission whereas the intensity of the low-energy tail increases with the angle normal to the surface in a way which depends on the projectile ion charge state. Interestingly, this low-energy component also shows a pronounced enhancement on detectors located in the projectile forward direction. Subtracting a time-of-flight distribution recorded in backward from one recorded in the forward direction produces a Gaussian component centered at a time of flight corresponding to 2 eV electrons (Fig. 6). It is suggested that this peak may be due to “convoy” electrons<sup>12</sup> following the scattered projectile or to pure “kinetic” emission from LiF.<sup>13</sup>

## 2. Electron statistics: Counting the electrons

To measure the secondary electron yield  $\gamma$ , one may simply count the number of electrons detected after the impact of an ion on the surface. In our case, as detailed above, the detection of a scattered particle indicates within few nanoseconds when the impact on the surface took place. Furthermore the above TOF spectra indicate that a 300 ns time window located after the impact time is wide enough to insure that all electrons have arrived. Indeed, we easily check that the number of detected electrons does not increase any further when the duration of this software time window is doubled. This is true also since, in our experimental conditions, the time window is smaller than the mean time between two successive ions by almost two orders of magnitude. The detection efficiency is determined both by geometric efficiency that is the angular coverage of the  $2\pi$  solid angle and by the detection efficiency of the MCP. Note also that this method has no intrinsic limitation to record events with no secondary electrons detected. A calibration of the data on the absolute yield as measured accurately by the Vienna<sup>2,5</sup> group would be possible if such data had been recorded with projectiles at grazing incidence.

On the other hand, the energy information in the electron time of flight allows an estimate for the detection efficiency. With  $O^{8+}$  as projectile, there is at most two transitions filling the  $K$  shell. For any scattered ion detected, we identify 25.8% of events with at least one such “ $K$ ” electron and 2.6% of events with two such “ $K$ ” electrons defined by a 7-ns-wide window in the spectra shown in Fig. 5. If both electrons are emitted outside the surface independently and detected with a probability  $P$  then the two values measured above correspond to  $2P(1-P)$  and  $P^2$ . These two independent measurements give  $P=15.2\%$  and  $16.1\%$ , respectively, with most of the uncertainty coming from an unambiguous identification of a “ $K$ ” electron. As detailed in Sec. II, the surface mapped by the 16 detector units is close to 50% but in this file only 13 were active for electron detection, taking into account the 85% transparency of the inner grid, we may conclude that, in the resulting 35% effective solid angle, the detection efficiency is 45%. This is a lower bound since it assumes that for each impact, two “ $K$ ” electrons are emitted, and that all electrons emitted toward the bulk are reflected outside as fast electrons.

The correlations between the electron energy and the electron statistics may also bring valuable information on the various emission mechanisms. For instance, once events with double  $K$  shell closing transition have been detected, we may compare the associated energy distribution and emission statistics with the corresponding noncoincident data. As a result, one may receive the contribution of these fast electrons when emitted into the bulk. This, however, requires a more accurate knowledge of the detection efficiency to compensate for those events where the electrons were emitted but not detected; this work is still in progress.

## 3. Correlation between secondary electrons and between electrons and ions

The specificity of the present tool lies in the possibility to correlate events recorded by the various detectors. Though

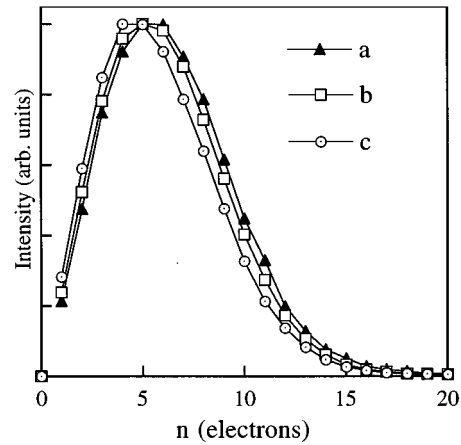


FIG. 7. Statistical distribution of the number of ejected electrons detected on the  $2\pi$  detector. The three curves correspond 32 keV  $O^{8+}$  ions colliding on LiF and scattered around (a)  $\theta \approx 6^\circ$ , (b)  $\theta \approx 3^\circ$ , (c)  $\theta \approx 1^\circ$ .

the above-described TOF spectra and statistics are already derived through multicoincidence events between scattered particles and secondary electrons, the general analysis of correlations in such a wide multidimensional space is mainly limited by the complexity in the interpretation and by the lack of well-established procedure. For instance, each recorded event describes a given autoionization cascade with probably strong correlation between all the, say, ten electrons detected. The analysis of properties (e.g., energy and angular distribution) of the correlated electrons would allow to check a given cascade model.

Several “simple” correlations can readily be looked for in the present data. For instance, one may wonder if the number of emitted electrons depends on the final charge state and/or the scattering angle of the reflected particles or if the number of emitted electrons depends on their energy? We observe that the secondary electron statistics depend weakly on the scattered projectile charge state, but the dependence on the projectile scattering angle is more pronounced (Fig. 7). The question now arises whether these findings correspond to different effects or not, since different scattered charge states show different scattering profiles. Selecting a given scattering angle, we have checked that the secondary electron yields are almost the same for all final charge states, so that the dependence on the scattered particle charge state is in fact associated with the scattering pattern of each final charge state. This simple example illustrates the power but also the amount of work needed to understand any observed correlation.

A second example of correlation is observed between the scattering pattern and the number of secondary electrons [Figs. 8(a) and 8(b)]. In surface or subsurface channeling conditions, the scattering pattern is drastically different whether taken in coincidence with a large number ( $n > 6$ ) of detected electrons [Fig. 8(a)] or with a low number of electrons [one or two, Fig. 8(b)]. In this last case, the side maxima of the “banana” shape dominate the profile whereas these maxima almost disappear when a large number of electrons is detected. This contrasting situation is also reflected in the correlation with scattering position and the energy loss

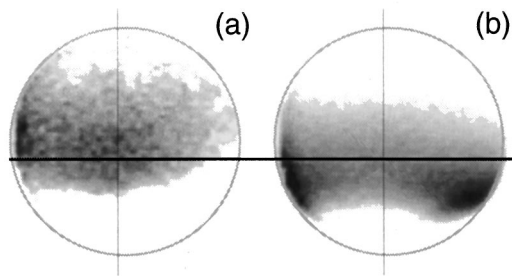


FIG. 8. Two-dimensional  $\theta, \phi$  pattern (vertical and horizontal axis, respectively) of the scattered particles for 16 keV  $\text{Ar}^{8+}$  colliding on LiF under channeling conditions and recorded in coincidence with a given number of secondary electrons detected on the  $2\pi$  device. (a) In coincidence with at least six secondary electrons and (b) in coincidence with less than three electrons. The vertical lines correspond to the incident plane ( $\phi=0$ ) and the horizontal lines correspond to the specular angle. The intensity enhancement close to the left border of pictures is due to ions reflected on the edge of the cylinder shielding the exit hole.

which is the largest both in the central part of the pattern and in case of coincidences with the larger number of secondary electrons. The detailed analysis will be presented in a forthcoming article.

### C. Sputtered ions

Since the MCP detectors have a floating collector, it is also possible to bias the entrance negatively, 1100 V relative to the target and inner sphere, in order to detect the slow positive ions sputtered out of the sample. The angular and energy distribution can be determined by TOF measurements on each individual detector triggered by the scattered particle. However, the secondary-ion energy distribution around few eV is so broad that the field-free TOF does not allow mass identification, provided that the ions have the same charge state. Actually the consistency of the results indicates that only singly charged ions are significantly produced. The mass spectrum is obtained by applying a positive voltage on the target to accelerate the positive ions. Few tens of volt are already large enough to allow a reasonable mass separation. In this mode the shape of the TOF peak associated with each well-resolved mass still allows accurate energy measurements. Figure 9 shows a secondary-ion time-of-flight spectrum recorded for 32 keV  $\text{Ar}^{16+}$  ions impinging on a LiF single-crystal target. The successive peaks are assigned to  $\text{Li}^+$ ,  $\text{Li}_2^+$ ,  $\text{F}^+$ ,  $\text{Li}_2\text{F}^+$ , and  $\text{Li}_n\text{F}_2^+$  (with  $n \leq 4$ ) secondary ions. The most interesting feature is the presence of Li molecular ions isolated ( $\text{Li}_2^+$  and  $\text{Li}_3^+$ ) or bound to fluorine atoms. The abundance of these species contrasts with the very low yield of fluorine ions (see, e.g., Ref. 13). This relatively high abundance of heavy molecular ions is probably underestimated since the post acceleration before the MCP detector was limited leading to a detection efficiency which rapidly decreases with the mass of the ions. The analysis of the pulse amplitude distribution associated with the detection of a given ion mass will certainly allow first-order corrections for the relative abundance's. It is worth noting that the absolute ion sputtering yield is remarkably large.<sup>14</sup> For instance, with  $\text{Ar}^{16+}$  as a projectile, almost one secondary ion per scattered particle is detected. The secondary-ion statistics has an ex-

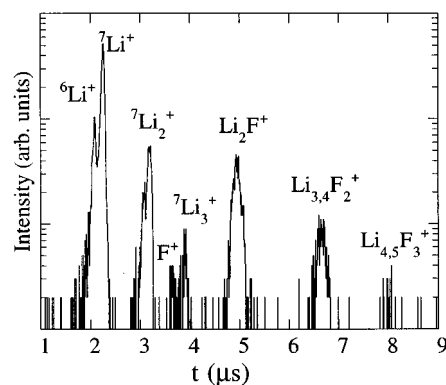


FIG. 9. TOF mass spectrum of the desorbed ions after the impact of 32 keV  $\text{Ar}^{16+}$  ions on LiF. This spectrum has been recorded on the topmost detector subunit and with the target biased at 80 V. It shows that lithium ions and various fluorine halide compounds are produced contrasting with the quasi-absence of fluorine atomic ions.

ponential shape which probably means that the ionic emission processes are independent. This could be due to the grazing incidence conditions where the electrons are captured by the projectile all along the incoming trajectory.

### D. On line diagnosing of the surface

Three different techniques have been used here to analyze the surface chemical composition and surface flatness.

#### 1. Chemical purity

The collision of highly charged ions on insulator surfaces at grazing incidence produces a very high secondary-ion yield. This allows for a wide dynamics in the mass spectra. The TOF spectrum in Fig. 9 shows only the presence of Li and F compounds. This is not the case if the target heating has been stopped even for few hours, in such case a  $\text{H}^+$  peak appears which will eventually dominate the whole spectrum. We did not see the presence of other impurities (neither really looked for) since LiF single crystal is known to be rather pure after several hours of heating above  $400^\circ$ . So far, this technique has been applied only for positive ion detection but the bias of the target to negative voltage should bring comparable information on the negative ion composition. Once again the technique is new and the specificity of grazing angle highly charged ions induced SIMS remains to be clarified.

#### 2. Crystalline orientation and surface roughness

The most straightforward diagnosing comes from the analysis of the scattering pattern for keV low charge-state projectiles. In case of a simple crystal structure, it has been very easy to find the principal surface channeling direction just by changing the azimuthal direction until the appearance of the typical scattering "banana" shape (see Fig. 8). Sensitive fine tuning is obtained in optimizing the symmetry of both sides of the banana. In a second step, the width of the profile may be used to monitor the surface flatness. In our case, this width rapidly decreases down to a degree FWHM after few hours of sputtering by 5 keV  $\text{Ar}^+$  at  $10^\circ$  incidence

angle and heating up to 400°. More work is needed to relate the observed width to the terrace size for instance.

### 3. Analysis of the direct recoil (DR)

The third on line diagnosing has not been described above and relies on the detection, on the  $2\pi$  detectors, of fast keV particles ejected from the surface. In “dirty” conditions, the “electron” TOF spectra show not only the electron signal but also a structure around one  $\mu\text{s}$  corresponding to fast neutral particles ejected from the surface. Those particles are emitted preferentially in the forward direction and can be interpreted as direct recoils (DR) originating from binary collisions on the surface (see, for instance, Ref. 15). Indeed we easily checked that the DR signal is very large until the surface is clean and decently flat according to the two above criteria. For these DR events, the scattering angle of the projectile is measured within  $0.1^\circ$  while the one of the direct recoil is known within  $\pm 7^\circ$ . This information, together with the TOF difference between both partners, turned out not to be sufficient to resolve the DR mass composition. This may be due to the poor angular resolution on the DR impact location. Furthermore, the present technique involving coincident detection of both partners outside the surface certainly requires additional collisions which break the pure binary collision model.

### ACKNOWLEDGMENTS

One of the authors (V.M.) thanks the CNRS for a temporary position. This work was supported by a European Union HCM project and by a Franco Russian collaboration program (PICS). They kindly acknowledge enlightening dis-

cussions with A. Borissov, R. Morgenstern, and HP Winter. They are grateful to A. Brenac, T. Lamy, G. Lamboley, and F. Gustavo for their assistance in running the ECR source at the AIM facilities (Grenoble).

- <sup>1</sup>M. Delaunay, M. Fehring, R. Geller, D. Hitz, P. Varga, and H. P. Winter, *Phys. Rev. B* **35**, 4232 (1987).
- <sup>2</sup>F. Aumayr, H. Kurz, D. Schneider, M. A. Briere, J. W. McDonald, C. E. Cunningham, and H. P. Winter, *Phys. Rev. Lett.* **71**, 1943 (1993).
- <sup>3</sup>F. W. Meyer, S. H. Overbury, C. C. Havener, P. A. Zeijmans van Emmichoven, and D. M. Zehner, *Phys. Rev. Lett.* **67**, 723 (1991); J. Das, L. Folkerts, and R. Morgenstern, *Phys. Rev. A* **45**, 4669 (1992); S. Schippers, S. Hustedt, W. Heiland, R. Kohrbruck, J. Bleck-Neuhaus, J. Kemmler, D. Lecler, and N. Stolterfoht, *ibid.* **46**, 4003 (1992).
- <sup>4</sup>J. P. Briand, L. de Billy, P. Charles, S. Esabaa, P. Briand, R. Geller, J. P. Desclaux, S. Bliman, and C. Ristori, *Phys. Rev. Lett.* **65**, 159 (1990); J. J. Bonnet, A. Fleury, M. Bonnefoy, M. Chassevent, T. Lamy, A. Brenac, A. Simionovici, H. J. Andrä, and S. Andriamonge, *Z. Phys. D* **21**, S343 (1991).
- <sup>5</sup>F. Aumayr, T. D. Mark, and H. P. Winter, *Int. J. Mass Spectrosc. Ion Processes* **129**, 17 (1993); H. Kurz, F. Aumayr, C. Lemell, K. Toghiofer, and H. P. Winter, *Phys. Rev. A* **48**, 2192 (1993).
- <sup>6</sup>L. Folkerts, S. Schippers, D. M. Zehner, and F. W. Meyer, *Phys. Rev. Lett.* **74**, 2204 (1995).
- <sup>7</sup>V. A. Abramenko, D. V. Ledyankin, I. F. Urazgil'din, and V. Urasova, *Nucl. Instrum. Methods B* **33**, 547 (1988).
- <sup>8</sup>V. A. Morosov, A. Kalinin, Z. Szilagyi, M. Barat, C. Benoit, M. N. Gaboriaud, and P. Roncin, *Nucl. Instrum. Methods B* **98**, 597 (1995).
- <sup>9</sup>H. Winter, in *XVIII ICPEAC Inv. Papers*, AIP No. 295, edited by T. Andersen, B. Fastrup, F. Folkmann, H. Knudsen, and N. O. Andersen (AIP, New York, 1993).
- <sup>10</sup>C. Auth, A. G. Borisov, and H. Winter, *Phys. Rev. Lett.* **75**, 2292 (1995).
- <sup>11</sup>J. J. C. Geerlings and J. Los, *Phys. Rep.* **190**, 133 (1990).
- <sup>12</sup>E. A. Sanchez, O. Grizzi, M. L. Martiarena, and V. H. Ponce, *Phys. Rev. Lett.* **71**, 801 (1993). C. O. Reinhold, J. Burgdorfer, J. Kemmler, and P. Koschar, *Phys. Rev. A* **45**, 2655 (1992).
- <sup>13</sup>W. König, K. H. Krebs, and S. Rogaschewski, *Int. J. Mass Spectrosc.* **16**, 243 (1975).
- <sup>14</sup>T. Neidhart, F. Pichler, F. Aumayr, H. P. Winter, M. Schmid, and P. Varga, *Phys. Rev. Lett.* **74**, 5280 (1995), and recent references included.
- <sup>15</sup>O. Grizzi, M. Shi, H. Bu, and J. W. Rabalais, *Rev. Sci. Instrum.* **61**, 740 (1990).